RSC Advances

PAPER

View Article Online
View Journal | View Issue

Cite this: *RSC Adv.*, 2025, **15**, 2444

Metal-free photocatalyst with reduced graphene oxide-doped graphitic carbon nitride homojunctions for efficient antibacterial applications†

Junyan Zhang, Weikun Wang, Shiyue Huang, Yijie Lv, Meilan Li, Mingliang Wu* and Haiyang Wang *

Received 3rd November 2024
Accepted 14th January 2025

DOI: 10.1039/d4ra07829b

rsc.li/rsc-advances

Bacterial infections are a major global health challenge, posing severe risks to human well-being. Although numerous strategies have been developed to combat bacterial pathogens, their practical application is often hindered by operational constraints. Photocatalytic materials have emerged as promising candidates for bacterial disinfection and food preservation due to their efficiency and sustainability. In this study, a graphitic carbon nitride (g-C_3N_4) homojunction was synthesized, with reduced graphene oxide (RGO) incorporated to suppress the rapid recombination of photocarriers. The resulting composites demonstrated significantly enhanced photocatalytic antibacterial activity compared to original g-C_3N_4. The improvement is due to the critical role of RGO, which not only facilitates efficient electron transport but also introduces sharp edges that mechanically disrupt bacterial cell membranes. The experimental results demonstrated that the composite exhibited a bactericidal efficiency of 99.92% against *Escherichia coli* and 99.85% against *Staphylococcus aureus* within 180 minutes, highlighting its potential for practical antibacterial applications.

1. Introduction

Harmful bacteria have become an increasingly serious hazard to human life and health, specifically in modern society, where globalization and urbanization have accelerated the diversification of transmission pathways.[1] These bacteria can cause various acute and chronic diseases, such as foodborne illnesses, respiratory infections, and tuberculosis.[2] They can also lead to antibiotic resistance, rendering traditional treatments ineffective.

Lately, the study and application of antimicrobial materials have become a focal point in the fields of public health and materials science.[3–5] Traditional antimicrobial materials, such as silver and copper-based compounds, have seen broad application because of their excellent antibacterial properties.[6–8] However, their long-term use may lead to issues such as antibiotic resistance and environmental pollution. In contrast, the application of photocatalysts and graphene-based materials offers unique advantages.[9–11] Graphitic-carbon-nitride (g-C_3N_4), a novel two-dimensional photocatalytic material,[12,13] features a graphite-like structure with tri-s-triazine units and a bandgap of approximately 2.7 eV.[14] It stands out for its low cost, good stability, and eco-friendliness.[15] Under light exposure, it can generate reactive oxygen species (ROS) with strong oxidative capability, achieving efficient antibacterial effects.[16] Its advantages include: (1) under sunlight or artificial light, photocatalysts can continuously exert antibacterial effects without easily inducing resistance; (2) the antibacterial mechanism is triggered by light activation, causing bacterial membrane disruption and intracellular material oxidation, which minimizes environmental impact.[17,18]

Fang *et al.* successfully fabricated phosphorus and sulfur co-doped carbon nitride nanosheets (PSCN) through high-temperature hydrothermal synthesis and liquid nitrogen exfoliation.[19] Compared to the original g-C_3N_4, PSCN exhibits significantly enhanced photocatalytic antibacterial performance. Upon visible-light, PSCN generates highly reactive species, such as h^+ and $^{\cdot}O_2^-$. Within 2.5 hours, its antibacterial rate against *Staphylococcus aureus* (*S. aureus*) reached 99.2%, and its antibacterial efficacy against *Escherichia coli* (*E. coli*) reached 97.0% within 2 hours. In addition to heteroatom doping, the construction of g-C_3N_4 homojunctions is another effective modification strategy that significantly enhances photocatalytic performance without introducing additional elements. Ma and co-workers anchored CN quantum dots (QDs) to g-C_3N_4, creating a homojunction.[20] Its outstanding efficiency is attributed to the energy level alignment of the homojunction,

College of Food Science and Technology, Jiangsu Agri-animal Husbandry Vocational College, Taizhou 225300, China. E-mail: Wanghaiyangwtc@163.com

† Electronic supplementary information (ESI) available. See DOI: https://doi.org/10.1039/d4ra07829b

which facilitates well photocarriers separation. Under visible light irradiation, HJ-C_3N_4 achieved an H_2O_2 production rate of 115 μmol L^{-1} h^{-1} in water, 8.6 times greater than that of g-C_3N_4. By constructing a homojunction, an internal electric field can be formed within the single material system, effectively promoting the separation of photocarriers and reducing their recombination rate, thereby significantly improving photocatalytic efficiency. Additionally, the formation of the homojunction can adjust the light absorption range of g-C_3N_4, enabling more efficient utilization of solar energy.

Additionally, graphene-derived materials have become a research hotspot as novel antibacterial materials due to their excellent conductivity, mechanical strength, and high specific-surface-area.[21,22] The antibacterial properties of graphene mainly arise from its unique two-dimensional structure, which can physically disrupt bacterial cell membranes and inhibit bacterial growth through surface adsorption mechanisms.[23] Moreover, the combination of graphene with other antimicrobial materials helps enhance its performance.[24–26]

Therefore, in this work, tightly bound g-C_3N_4 homojunction (UCN/SCN) were obtained through one-step calcination using two carbon-nitrogen precursor materials. Furthermore, reduced graphene oxide (RGO) composite materials (UCN/RGO/SCN) were synthesized by one-step high-temperature calcination of GO with the two g-C_3N_4 precursors. The results show that, compared to single g-C_3N_4 materials (UCN and SCN), both the homojunction UCN/SCN and the RGO-doped UCN/RGO/SCN exhibit significantly enhanced carrier separation rates. Additionally, the incorporation of RGO improves the charge transfer rate across interfaces. Under simulated sunlight irradiation, *E. coli* and *S. aureus* was selected as the test subject to investigate the photocatalytic antibacterial efficiency, as well as the influence of irradiation time on their antibacterial efficacy. The results indicate that the RGO-doped heterojunction UCN/RGO/SCN demonstrates superior antibacterial performance compared to the other materials. The observed enhancement in antibacterial performance in this study can be attributed to several factors. First, the homojunction structure (UCN/SCN) effectively boosts the separation of photocarriers, reducing electron–hole recombination and optimizing carrier transport, thus enhancing the performance of photocatalytic processes. Second, the introduction of reduced graphene oxide (RGO) significantly increases the charge conduction rate across the interfaces, facilitating the movement of electrons within the material. Additionally, the sharp edges of RGO lead to cell inactivation, further improving antibacterial effectiveness. Under light irradiation, the composite material generates more active species, like hydroxyl radicals ($^{\bullet}OH$) and superoxide anions ($^{\bullet}O_2^-$), which have a strong oxidative destructive effect on bacterial cell membranes, thus enhancing antibacterial performance.

2. Experimental methods and details

2.1. Catalyst preparation

2.1.1. Preparation of UCN. 10 g of urea was placed in a 550 °C tubular furnace under continuous Ar flow, with a temperature increase of 5 °C per minute and a duration of 4 h. Upon reaching room temperature, the obtained material was gathered and denoted as UCN.

2.1.2. Preparation of SCN. Similar to the preparation of UCN, except that 10 g of thiourea was used as the raw material instead of urea.

2.1.3. Preparation of UCN/SCN. 5 g of urea and 5 g of thiourea were placed in a tubular furnace at 550 °C under continuous Ar flow, with a temperature increase of 5 °C per minute and a duration of 4 h. Upon reaching room temperature, the obtained material was gathered and denoted as UCN/SCN.

2.1.4. Preparation of UCN/RGO/SCN. First, 5 g urea and 5 g thiourea were dissolved in 15 mL water. Then, 200 μL of 16.8 mg L^{-1} graphene oxide (GO) solution was slowly added to the mixture. The resulting solution was placed in an 80 °C water bath to evaporate. The subsequent steps are the same as those mentioned above. The obtained material was gathered and denoted as UCN/RGO/SCN.

2.1.5. Preparation of UCN/RGO. Similar to the preparation of UCN/RGO/SCN, except that 10 g of urea was chosen as the base material instead of the mixture of urea and thiourea.

2.1.6. Preparation of SCN/RGO. Similar to the preparation of UCN/RGO/SCN, except that 10 g of thiourea was used as the raw material.

2.2. Characterization

The crystal structure of the materials was examined using a D8 Advance polycrystalline X-ray diffractometer (XRD) (Bruker AXS, Germany). The morphology was observed using a field emission scanning electron microscope (SEM) (GeminiSEM 300, Carl Zeiss, Germany). The chemical moieties were analyzed using an infrared spectrometer (IR) (Cary 610/670, Varian, America). The chemical composition, chemical state, and valence band position were analyzed by Thermo Scientific Nexsa G2 X-ray photoelectron spectrometer (XPS). Photoluminescence spectra was analyzed using a spectrofluorometer (F-4500, Hitachi, Japan). Electrochemical impedance spectra (EIS) and transient photocurrent were performed on an electrochemical workstation (CHI660B, Shanghai Chenhua Co., China) with a three-electrode system. 0.5 mol L^{-1} Na_2SO_4 solution was employed as the electrolyte. EIS was conducted by applying 5 mV alternating signal with a frequency of 100 kHz – 0.01 Hz.

2.3. Photocatalytic antibacterial experiment

Escherichia coli (*E. coli*) was chosen as the target bacterial strain for the photocatalytic disinfection experiment. The bacteria were cultured in Luria-Bertani (LB) nutrient broth for 12 h until they reached the logarithmic growth phase, which was monitored by measuring the OD600 value using a nucleic acid/protein analyzer. A 2 mL bacterial suspension was collected. The bacterial pellet was then washed twice with phosphate-buffered saline (PBS) and resuspended in PBS solution. The final concentration of the bacterial suspension was roughly 1×10^7 CFU mL^{-1}.

In the photocatalytic disinfection experiment, the 300 W xenon lamp with a 400 nm filter was used (light intensity nearly

100 mW cm^{-2}). Before the experiment, the equipment and materials were sterilized at 121 °C for 20 min and subjected to UV sterilization for 30 min. 20 mg photocatalyst was added to 20 mL PBS containing 400 μL of bacterial suspension. The bacterial concentration at different time intervals was measured by standard plate counting techniques.

For comparison, control experiments were performed under the same conditions: one with the photocatalyst in the dark and another under light without the photocatalyst. During the photocatalytic experiment, using a magnetic stirrer for continuous stirring. To avoid temperature effects, reaction were carried out in an ice water bath. Each disinfection test was repeated three times.

3. Results and discussion

The synthesis route was shown in the Fig. 1. Different g-C_3N_4 precursors and GO were subjected to a one-step calcination process to prepare RGO-doped g-C_3N_4 homojunctions (UCN/RGO/SCN). Fig. 2a illustrates the crystal structure of the samples as verified by XRD. The distinct peaks at 13.5° (100) and 27.3° (002) were correspond to the planar structural stacking of triazine units and the interlayer stacking of conjugated aromatic rings, respectively (JCPDS 87-1526).[27,28] It can be noted that the peak intensity at 27.3° differs significantly between UCN and SCN, with the peak intensity of SCN being significantly higher than that of UCN. This suggests that structural variations exist in g-C_3N_4 synthesized from various precursors, with SCN prepared from thiourea exhibiting a smaller interlayer spacing than UCN. This suggests that UCN may retain a looser structure.

When GO is added and calcined with the precursors, the resulting composite material UCN/RGO/SCN maintains a peak shape aligned with that of g-C_3N_4, suggesting that it retains the triazine ring structure. However, the peak intensities changes, indicating that the RGO affects the interlayer arrangement of aromatic rings to some extent.

FT-IR was used to identify the structure and functional groups of compounds. As depicted in Fig. 2b, the peak nearly 810 cm^{-1} is typically associated with the breathing mode in g-C_3N_4, specifically due to the vibrations of the s-triazine rings.[29] This peak is generally considered a characteristic feature of carbon nitride. Additionally, the 1200–1700 cm^{-1} peaks are usually linked with the stretching vibrations of the heterocyclic C–N and C=N bonds. The 3000–3500 cm^{-1} peaks are typically linked to the N–H vibrations of amino groups (–NH_2) or hydrogen-bonded N–H present on the surface of the sample,[30,31]

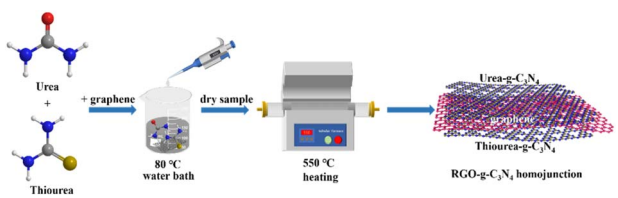

Fig. 1 Schematic illustration of the synthesis route for UCN/RGO/SCN.

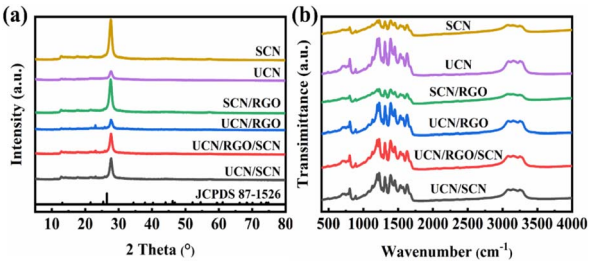

Fig. 2 (a) XRD and (b) FT-IR spectra of samples.

which often indicates residual moisture or surface amino groups in the sample. The differences in peak intensity for g-C_3N_4 prepared from different precursors suggest a variation in the number of surface functional groups. Upon doping with RGO, although there are changes in peak intensity, the peak shape remains unchanged, indicating that the UCN/RGO/SCN composite still retains the basic structure of CN.

The micro-morphology of the samples was observed using SEM. In Fig. 3a, the morphology of UCN is composed of a porous, sheet-like stacked structure. In contrast, Fig. 3b shows that SCN is formed by the stacking of large, flat layers, resulting in a relatively smooth surface. This suggests that UCN may have a relatively loose interlayer spacing, while the interlayer structure of SCN is more compact, consistent with the conclusions drawn from the XRD results mentioned earlier. When UCN/SCN was obtained by one-step calcination of the two precursors, its morphology remained a blocky stack, with a looseness that falls between UCN and SCN (Fig. 3c). After the addition of RGO, the morphology underwent a significant change. We observed large folded block structures (Fig. 3d), which could be due to the increased carbon content, leading to a tighter connection between the homostructures.

The chemical composition and element states of the materials were analyzed using XPS, providing detailed insights into the changes after incorporating RGO. In Fig. 4a, the C 1s XPS spectrum presents three peaks at 284.80, 286.43, and 287.95 eV, corresponding to C–C bonds in the s-triazine ring, C=N bonds,

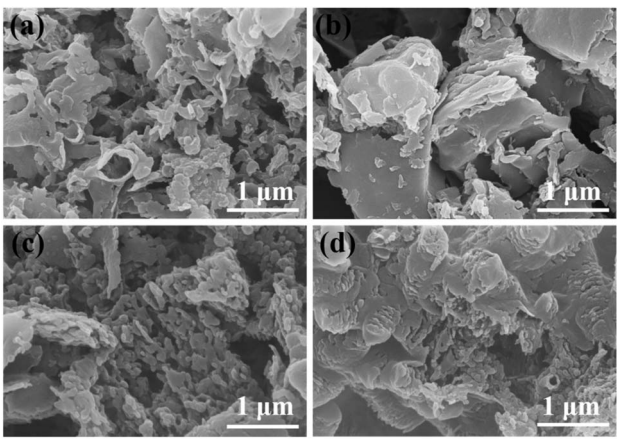

Fig. 3 SEM images of (a) UCN (b) SCN (C) UCN/SCN and (d) UCN/RGO/SCN.

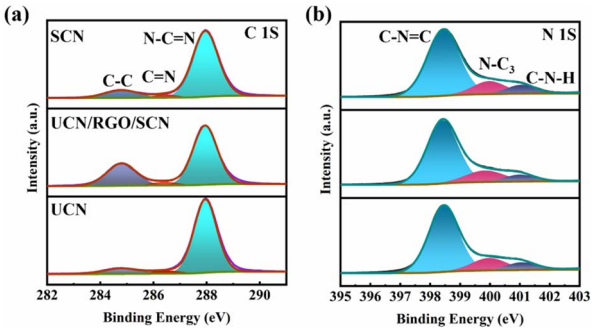

Fig. 4 XPS spectra of (a) C 1s and (b) N 1s of UCN, UCN/RGO/SCN and SCN.

and N–C=N bonds, respectively.[32,33] Fig. 4b illustrates three peaks at nearly 398.46, 399.97, and 401.05 eV, attributed to C–N=C, N–$(C)_3$, and C–N–H bonds, respectively.[34,35] In comparison to the individual UCN and SCN, the C and N 1s peaks of the UCN/RGO/SCN composite exhibit similar characteristics, indicating that the composite still retains the basic 3-s-triazine framework structure of the CN. However, in the C 1s spectrum, the intensity of the C–C peak corresponding to the foreign carbon is notably enhanced, which is indicative of the successful incorporation of carbon from RGO.

The optical absorption characteristics of the materials were evaluated using UV-vis-NIR absorption spectroscopy. In the Fig. 5a, SCN exhibits a significantly stronger light response compared to UCN. After doping with RGO, the light absorption performance of both materials is notably improved, surpassing that of the original SCN and UCN.

Among the various composite materials, UCN/RGO/SCN demonstrates superior light absorption capability compared to UCN/RGO and SCN/RGO. This enhanced absorption is linked to the construction of the homojunction and the doping of reduced graphene oxide (RGO). The experimental results indicate that RGO doping effectively enhances the catalyst's light absorption capacity, which is crucial for improving solar energy utilization and ultimately accelerating the photocatalytic activity. In photocatalytic experiments, this improvement allows the photocatalytic materials to better absorb light in the visible spectrum.

Based on the UV-vis-NIR absorption spectra, the bandgap values (E_g) were calculated using the formula $\alpha h\nu = A(h\nu - E_g)^{n/2}$.[36] The calculated bandgap values for UCN and SCN are 2.64 eV and 2.55 eV, respectively (Fig. 5b). Additionally, according to the XPS results of the valence band (VB), the VB levels of UCN and SCN are 1.83 eV and 1.97 eV (Fig. 5c and d), respectively. The conduction band (CB) can be calculated using the formula: $E = E_g - E_{VB}$.[37] Therefore, the CB positions of UCN and SCN are −0.81 eV and −0.58 eV, respectively.

Through PL spectroscopy, the behavior of photocarriers generated by the photocatalyst under light irradiation can be observed, helping to understand their separation efficiency and recombination rate.[38] As shown in the Fig. S1,† the single UCN and SCN catalysts exhibit the highest intensity at 440 nm. In contrast, the PL peak of the composite material UCN/RGO/SCN is notably decreased, implying that the construction of the heterojunction and doping with reduced graphene oxide (RGO) can markedly improve carrier separation efficiency. The PL results indicate that during the reaction process, UCN/RGO/SCN involves more photo-generated electrons in the reaction, which is consistent with its superior photocatalytic antibacterial activity.

Improving charge transfer efficiency is crucial for constructing efficient photocatalysts.[39] Electrochemical impedance spectroscopy (EIS) could be used to evaluate the charge transfer efficiency of materials. The Fig. 6a shows the Nyquist plots of the materials tested under illumination. The UCN/RGO/SCN composite material has a smaller semicircle radius compared to UCN and SCN. This is because the doping of carbon enhances the charge transfer capability of the catalyst, suggesting that the resistance to photo-electron transfer throughout the UCN/RGO/SCN is significantly lower than in other samples. This results in a notable increase in the transfer efficiency of photocarriers in the composite material doped with graphene oxide.

To further elucidate the photocarriers separation characteristics of the UCN/RGO/SCN, transient photocurrent measurements were conducted. Materials with higher photocurrent, which serve as the driving units for photocatalytic reactions,

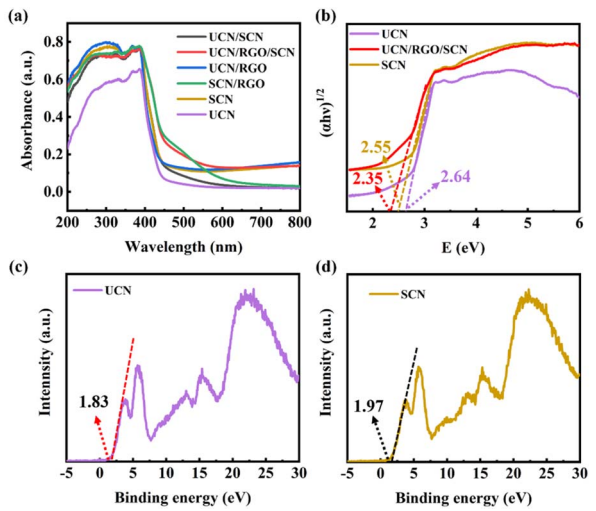

Fig. 5 (a) UV-visible diffuse reflectance spectra of different samples, (b) Tauc plot for UCN, SCN and UCN/RGO/SCN VB XPS spectra of (c) UCN and (d) SCN.

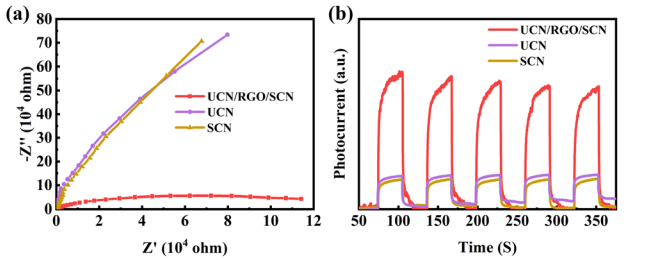

Fig. 6 (a) Electrochemical impedance spectra and (b) transient photocurrent responses of UCN, SCN and UCN/RGO/SCN.

typically exhibit higher electron–hole separation efficiency. This, in turn, is closely related to the longevity of photocarriers.[40] In the Fig. 6b, a comparison of UCN/RGO/SCN with pure UCN and SCN reveals that the composite material doped with graphene oxide shows the most significant carrier separation capability. This is ascribed to the well conductivity of graphene, which enhances electron transfer between interfaces. Additionally, the homojunctions formed by UCN and SCN are connected by graphene oxide to create a solid-state heterojunction, which accelerates the efficient separation of photocarriers and facilitates interfacial charge transfer.

4. Photocatalytic antibacterial performance evaluation

To investigate the impact of photocatalysts on antibacterial performance, a dark control group, a pure light irradiation control group, and a photocatalytic experimental group were set up. The Fig. 7a and b shows the condition of *E. coli* in both the control and experimental groups after 180 minutes of visible light irradiation. The antibacterial rates for UCN, SCN, UCN/SCN, UCN/RGO, SCN/RGO, and UCN/SCN/RGO were 58.12%, 51.34%, 84.21%, 93.26%, 88.63%, and 99.92%, respectively. The effect of photocatalyst dosage on antibacterial performance was also investigated (Fig. 7c), and it was observed that increasing the dosage improves efficiency up to a point. When the dosage exceeds 1.0 g L^{-1}, the improvement plateaus. This is likely due to the aggregation of excess catalyst particles, which causes light scattering and shielding, reducing effective light absorption and limiting photocatalytic activity.[41]

The antibacterial performance of UCN/RGO/SCN against *S. aureus* was further investigated. As shown in the Fig. 7d, its antibacterial efficiency reached 99.85% at 180 minutes. Fig. 7e illustrates the monitoring results of the antibacterial process, where a significant reduction in bacterial colonies over time was observed through bacterial suspension culturing. This demonstrates that the material exhibits excellent antibacterial efficacy against both *E. coli* and *S. aureus*.

Simultaneously, the morphological alterations of bacteria were observed using SEM, as depicted in the Fig. 8a and b. *E. coli* exhibited an intact morphology before treatment, while after photocatalysis, the cells showed signs of shrinkage. The incomplete cell structure further confirmed irreversible cell damage. Considering the morphological changes, it can be inferred that the ROS generated by the UCN/SCN/RGO composite played a role in the death of *E. coli* and the leakage of cytoplasmic contents.

The live and dead bacteria after sterilization were observed using a laser scanning confocal microscope, and the results are shown in the Fig. 8c. DMAO stains live bacteria with intact cell membranes, emitting green fluorescence, while PI stains dead bacteria with damaged cell membranes, emitting red fluorescence. In the absence of photocatalyst and light exposure, the bacterial cells exhibited strong green fluorescence with minimal red fluorescence. After photocatalytic treatment, a large amount of red fluorescence appeared in the bacterial cells, indicating that the bacteria were extensively inactivated under the UCN/RGO/SCN photocatalytic action.

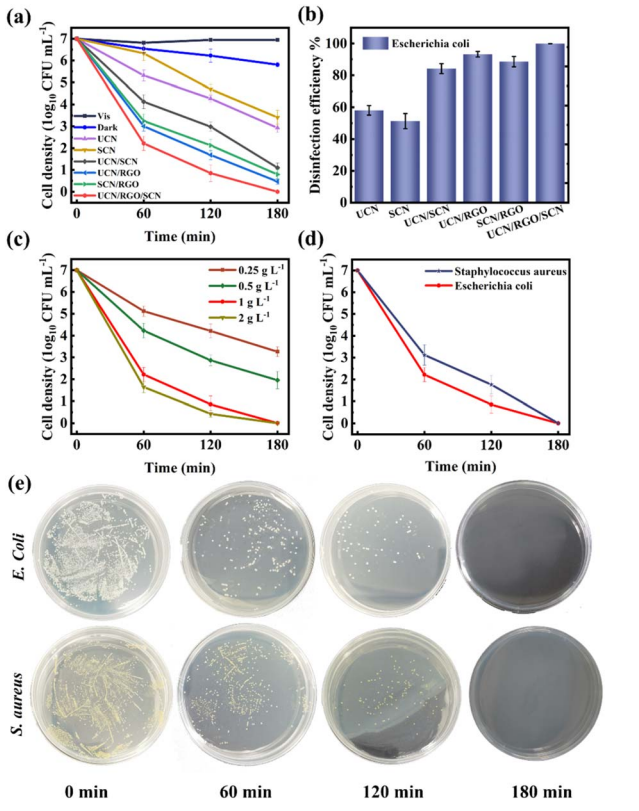

Fig. 7 (a and b) Photocatalytic antibacterial efficiency of *E. coli* by the control group and different photocatalysts. (c) Effect of catalyst concentration on antibacterial activity against *E. coli*. (d) Comparison of antibacterial performance against different bacteria (e) Coated plates showing results for *E. coli* and *S. aureus* using UCN/RGO/SCN.

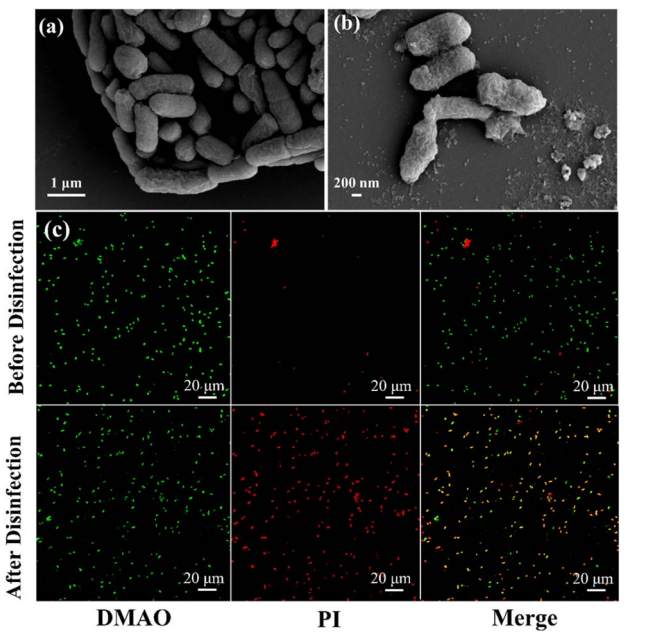

Fig. 8 SEM images of *E. coli* (a) before and (b) after antibacterial treatment. (c) DMAO/PI-mediated live/dead assay of *E. coli* cells.

Under dark conditions with the addition of the photocatalyst, the number of bacterial colonies decreased, with a bacterial mortality rate of 16.97% (Fig. 7a), indicating that UCN/SCN/RGO exhibited certain bactericidal ability. SEM observations revealed that (Fig. S2†), compared to the original *E. coli*, the bacteria treated in the dark displayed noticeable wrinkles and some surface damage. This suggests that the bacterial cell membrane may have been affected, possibly due to the sharp edges of the reduced graphene oxide (RGO) material making contact with the bacterial surface, leading to physical damage. The sharp structures of RGO may interact with the bacterial membrane, causing localized damage, thereby affecting the cell's structure. Such physical effects caused by the surface morphology of nanomaterials have been reported in previous studies,[42–44] indicating that nanomaterials can cause localized disruption of bacterial membranes through direct contact, which in turn impacts bacterial survival.

After 180 minutes of light irradiation, the number of colonies in the UCN/SCN/RGO group was markedly reduced against the UCN and SCN groups. The reasons for this are twofold: firstly, the addition of RGO introduces sharp edges that directly damage bacteria; secondly, the formation of homojunctions in UCN and SCN suppresses charge carrier recombination, while the inclusion of RGO promotes charge transfer at the interface. This allows more electrons and holes to react with O_2 and H_2O to generate ROS, thereby achieving excellent antibacterial performance.

Next, the durability of the photocatalyst was assessed. The results are shown in the Fig. 9a. After five cycles, the composite material maintained a high antibacterial rate against *E. coli*. As depicted in Fig. 9b, the unchanged FTIR peak shape suggests that the chemical structure and major functional groups of the material remain intact, indicating its chemical stability during the reaction process. However, the overall decrease in peak intensity could be attributed to the adsorption of reaction residues on the surface of the photocatalyst. While these adsorbed substances may not significantly impact the active sites of the photocatalyst, they could obscure or weaken certain characteristic peaks during FTIR analysis, thereby leading to a reduction in the observed signal intensity.

To demonstrate the importance of ROS in photocatalytic antibacterial activity, radical scavenging tests were conducted. In the experiments, *tert*-butyl alcohol (TBA) and benzoquinone (BQ) were added to the mixed solution of the photocatalyst and bacterial suspension as scavengers for $^{\bullet}OH$ and $^{\bullet}O_2^-$.[45] As depicted in Fig. S3,† the antibacterial performance was significantly inhibited after the addition of TBA, suggesting that $^{\bullet}OH$ plays a crucial role in the disinfection process. Additionally, the sterilization efficiency is also partially suppressed when BQ was added, indicating that $^{\bullet}O_2^-$ contributes significantly to the reaction system. These results further confirm the synergistic effect of $^{\bullet}OH$ and $^{\bullet}O_2^-$ in the photocatalytic antibacterial process, providing evidence for a deeper understanding of the role of active species in antibacterial action.

Through ESR analysis of radical generation and transfer mechanisms, the production of $^{\bullet}O_2^-$and $^{\bullet}OH$ was detected using 5,5-dimethyl-1-pyrroline N-oxide (DMPO).[46] The experimental results are depicted in the Fig. 9. It indicates that under dark conditions, the characteristic signal of DMPO-$^{\bullet}O_2^-$ is almost undetectable (Fig. 10a), suggesting that neither UCN/RGO/SCN nor UCN/SCN produce O_2^- in the dark. However, as shown in Fig. 10b, when exposed to light, both UCN/RGO/SCN and UCN/SCN exhibit DMPO-$^{\bullet}O_2^-$ signals with an intensity ratio of 1 : 1 : 1 : 1, indicating that both can generate $^{\bullet}O_2^-$ under illumination, with UCN/RGO/SCN showing a significantly stronger signal. This further confirms that the inclusion of GO helps suppress the recombination of electron–hole pairs, leading to a higher reduction of O_2 to O_2^- in the system.

The Fig. 10c and d shows the DMPO$^{\bullet}$-OH EPR spectra, where no signal peaks appear under dark conditions, indicating that neither UCN/RGO/SCN nor UCN/SCN generate $^{\bullet}OH$ in the dark (Fig. 10c). Upon illumination, strong signals with an intensity ratio of 1 : 2 : 2 : 1 are observed (Fig. 10d). This indicates that both UCN/RGO/SCN and UCN/SCN can generate $^{\bullet}OH$ under light, with UCN/RGO/SCN displaying a significantly stronger signal. This further confirms that the addition of RGO enhances the carrier separation rate.

Since the reduction potential of $O_2/^{\bullet}O_2^-$ is −0.33 eV (*vs.* NHE) and the oxidation–reduction potential of $OH^-/^{\bullet}OH$ is

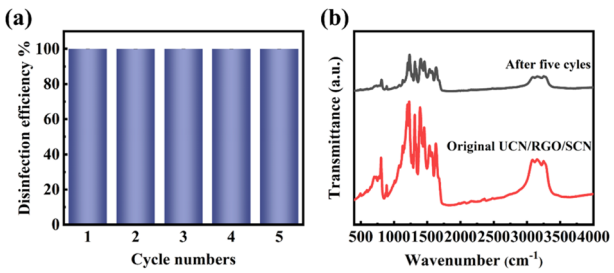

Fig. 9 (a) Continuous cycling photocatalytic antibacterial performance of UCN/RGO/SCN and (b) FT-IR spectra of UCN/RGO/SCN before and after the reaction.

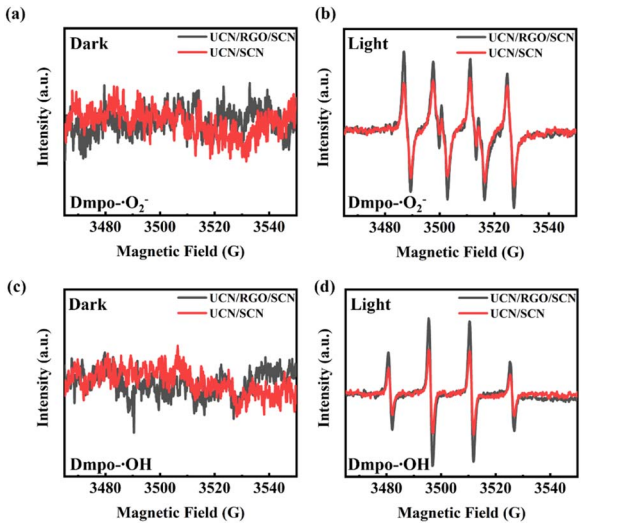

Fig. 10 EPR spectra of DMPO-$^{\bullet}O_2^-$ of UCN/SCN and UCN/RGO/SCN (a) in the dark and (b) in the light. EPR spectra of DMPO-$^{\bullet}OH$ radicals of UCN/SCN and UCN/RGO/SCN (c) in the dark and (d) in the light.

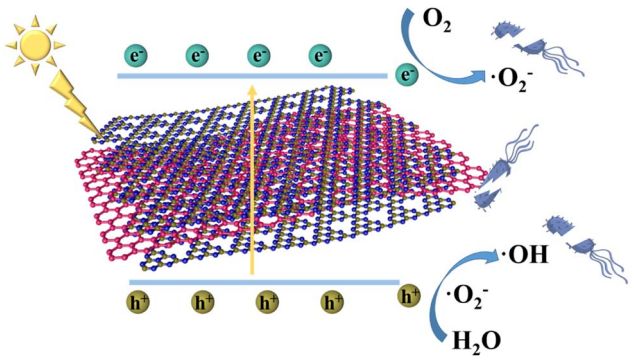

Fig. 11 Schematic illustration of the antibacterial mechanism of UCN/RGO/SCN under visible light.

2.38 V (*vs.* NHE),[47] electrons with reduction capability transferred to RGO can capture and reduce O_2 molecules to O_2^-. However, the h^+ could not directly oxidize OH^- or H_2O to $^{\cdot}OH$ but can further react with $^{\cdot}O_2^-$ to produce $^{\cdot}OH$. Under the action of these active radicals, the cell membranes of *E. coli* break, leading to bacterial death. These experimental results confirm that UCN/RGO/SCN can produce $^{\cdot}O_2^-$ and $^{\cdot}OH$ during photocatalysis, and the introduction of RGO results in a higher quantity of radicals produced.

The Fig. 11 shows the schematic of antibacterial activity for UCN/RGO/SCN under visible-light irradiation. Upon illumination, electron–hole pairs are separated. Compared to single UCN and SCN, the homojunction structure of UCN/SCN facilitates spatial separation of photocarriers, increasing the number of electron–hole pairs. With the introduction of RGO, more photo-electrons are transferred to the RGO surface, further accelerating carriers separation. Under the reduction action of electrons, O_2 was converted to $^{\cdot}O_2^-$, which can further transform into $^{\cdot}OH$ under the action of holes. Therefore, under the action of these active radicals, bacteria can be effectively killed.

To evaluate the toxicity of UCN/RGO/SCN on mammalian cell lines, a CCK-8-based cytotoxicity assay was conducted. The results were presented as the relationship between catalyst concentration and cell survival rate (Fig. S4†). At a concentration of 2 mg mL^{-1}, over 80% of mouse fibroblast cells (L929) remained viable. According to existing literature standards, a cell viability above 70% is typically considered safe, while values below this threshold may indicate potential cytotoxicity.[48] This result is particularly significant because fibroblasts are the primary cell type in animal connective tissue, responsible for synthesizing and secreting fibers and the extracellular matrix. These components play a crucial role in wound healing and tissue support.[49]

5. Conclusions

In summary, a novel metal-free photocatalyst with RGO-doped g-C_3N_4 homojunctions has been successfully fabricated for efficient disinfection. Notably, the doping of RGO significantly enhances the migration efficiency of photo-electrons while suppressing the recombination of photocarriers, thereby improving photocatalytic performance. Additionally, the sharp edges of RGO can disrupt cell membranes, further enhancing the antibacterial efficacy of UCN/RGO/SCN. The UCN/RGO/SCN photocatalyst achieved a high photocatalytic disinfection rate of 99.92% against *E. coli* and 99.85% against *S. aureus* within 180 minutes. The stability and environmental friendliness of UCN/RGO/SCN materials give them great potential for practical applications. They not only provide new insights for the development of metal-free antibacterial materials but also offer effective solutions for future public health and environmental protection.

Data availability

Data will be made available on request.

Author contributions

Junyan Zhang: conceptualization, supervision, project administration, writing-review & editing; Weikun Wang: investigation, visualization, formal analysis; Shiyue Huang: investigation, formal analysis; Yijie Lv: investigation, formal analysis; Meilan Li: investigation, formal analysis; Mingliang Wu: methodology, validation, formal analysis; Haiyang Wang: formal analysis, validation, supervision, project administration, writing – review & editing.

Conflicts of interest

There are no conflicts to declare.

Acknowledgements

The authors acknowledge Jiangsu Agri-animal Husbandry Vocational College scientific research project (number NSF2023ZR20).

References

1 C. Zhang, Y. Li, D. Shuai, Y. Shen and D. Wang, *Chem. Eng. J.*, 2019, **355**, 399–415.
2 Y. Liu, X. Zeng, X. Hu, J. Hu and X. Zhang, *J. Chem. Technol. Biotechnol.*, 2019, **94**, 22–37.
3 T. T. Deng, L. N. Lv, X. Y. Li, J. Wen, H. Li, H. Peng, H. Chen, C. Liu, L. G. Bao, C. P. Dang, Y. H. You and F. T. Chi, *Sep. Purif. Technol.*, 2025, **356**, 129610.
4 J. J. Wu, Y. Zhang, F. Y. Zhang, S. Mi, W. L. Yu, Y. X. Sang and X. H. Wang, *Food Chem.*, 2025, **463**, 141442.
5 J. M. He, W. L. Zhang, G. Goksen, M. R. Khan, N. Ahmad and X. L. Cong, *Food Chem.:X*, 2024, **24**, 101842.
6 M. Samir, S. A. Al Kiey, H. H. A. Rokbaa, S. El-Sherbiny and M. S. Hasanin, *Mater. Chem. Phys.*, 2024, **328**, 129974.
7 M. Assis, J. R. Santos, M. H. L. Cipriano, R. Y. N. Reis, L. K. Ribeiro, L. H. Mascaro, E. Longo and J. Andrés, *Surf. Interfaces*, 2024, **53**, 105074.
8 O. Bakina, L. Ivanova, A. Miller and A. Rechkunova, *J. Cluster Sci.*, 2024, **35**, 2871–2883.

9 Y. Ding, G. Yang, S. Zheng, X. Gao, Z. Xiang, M. Gao, C. Wang, M. Liu and J. Zhong, *J. Environ. Manage.*, 2024, **366**, 121875.
10 H. Yang, D. Y. He, C. H. Liu, X. X. Zhou and J. Qu, *Sep. Purif. Technol.*, 2023, **325**, 124697.
11 L. Caselli, T. Traini, S. Micciulla, F. Sebastiani, S. Koehler, E. M. Nielsen, R. G. Diedrichsen, M. W. A. Skoda and M. Malmsten, *Adv. Funct. Mater.*, 2024, **34**, 2405047.
12 X. X. Yang, L. A. Sheng, Y. L. Ye, J. D. Sun, J. Ji, S. X. Geng, D. L. Ning, Y. Z. Zhang and X. L. Sun, *Int. J. Biol. Macromol.*, 2024, **272**, 132834.
13 J. H. Thurston, N. M. Hunter, L. J. Wayment and K. A. Cornell, *J. Colloid Interface Sci.*, 2017, **505**, 910–918.
14 Y. F. Li, M. H. Zhou, B. Cheng and Y. Shao, *J. Mater. Sci. Technol.*, 2020, **56**, 1–17.
15 F. He, Z. X. Wang, Y. X. Li, S. Q. Peng and B. Liu, *Appl. Catal., B*, 2020, **269**, 118828.
16 Y. Li, Y. N. Li, S. L. Ma, P. F. Wang, Q. L. Hou, J. J. Han and S. H. Zhan, *J. Hazard. Mater.*, 2017, **338**, 33–46.
17 J. N. Guo, J. M. Zhou, Z. Sun, M. Y. Wang, X. Y. Zou, H. L. Mao and F. Yan, *Acta Biomater.*, 2022, **146**, 370–384.
18 B. B. Wu, Y. Li, K. Su, L. Tan, X. M. Liu, Z. D. Cui, X. J. Yang, Y. Q. Liang, Z. Y. Li, S. L. Zhu, K. W. K. Yeung and S. L. Wu, *J. Hazard. Mater.*, 2019, **377**, 227–236.
19 Y. R. Fang, S. L. Pei, L. Zhuo, P. Cheng, H. Yuan and L. S. Zhang, *Appl. Surf. Sci.*, 2022, **586**, 152761.
20 P. Ma, X. Zhang, C. Wang, Z. Wang, K. Wang, Y. Feng, J. Wang, Y. Zhai, J. Deng, L. Wang and K. Zheng, *Appl. Catal., B*, 2022, **300**, 120736.
21 H. Mohammed, A. Kumar, E. Bekyarova, Y. Al-Hadeethi, X. X. Zhang, M. G. Chen, M. S. Ansari, A. Cochis and L. Rimondini, *Front. bioeng. biotechnol.*, 2020, **8**, 465.
22 P. Kumar, P. P. Huo, R. Z. Zhang and B. Liu, *Nanomaterials*, 2019, **9**, 737.
23 V. Dutta, P. Singh, P. Shandilya, S. Sharma, P. Raizada, A. K. Saini, V. K. Gupta, A. Hosseini-Bandegharaei, S. Agarwal and A. Rahmani-Sani, *J. Environ. Chem. Eng.*, 2019, **7**, 103132.
24 Fauzia, M. A. Khan, A. Parveen, A. Almohammedi and A. Azam, *Opt. Quantum Electron.*, 2024, **56**, 1422.
25 L. Sung, T. Du, C. Hu, J. N. Chen, J. Lu, Z. C. Lu and H. Y. Han, *ACS Sustain. Chem. Eng.*, 2017, **5**, 8693–8701.
26 S. Arasavilli, P. A. Taksal, B. K. Das, S. Chowdhury and J. Bhattacharya, *J. Environ. Chem. Eng.*, 2024, **12**, 112703.
27 J. Fan, M. Zuo, Z. Ding, Z. Zhao, J. Liu and B. Sun, *Chem. Eng. J.*, 2020, **396**, 125263.
28 Z. Qiao, W. Chu, H. Zhou, C. Peng, Z. Guan, J. Wu, S. Yoriya, P. He, H. Zhang and Y. Qi, *Sci. Total Environ.*, 2023, **872**, 162309.
29 Z. P. Zhou, H. Zeng, L. Li, R. D. Tang, C. Y. Feng, D. X. Gong, Y. Huang and Y. C. Deng, *Water Res.*, 2024, **255**, 121521.
30 L. Zhang, X. Y. Zhou, S. X. Liu, H. Liu, S. Zhu, Y. Y. Mao, Q. Yang, S. Zhu, C. G. Zhang, T. Y. Wang and C. Y. Wang, *J. Cleaner Prod.*, 2023, **425**, 138912.
31 R. T. Li, T. Y. Gao, Y. Wang, Y. Chen, W. Luo, Y. Wu, Y. Xie, Y. Wang and Y. F. Zhang, *Int. J. Hydrogen Energy*, 2024, **63**, 1116–1127.
32 J. L. Sun, H. Z. Wu, C. H. Fu, C. H. Zhang, Z. Z. Hu and M. H. Zhou, *Appl. Catal., B*, 2024, **351**, 123976.
33 Z. Zhu, X. H. Xing, Q. Qi, W. J. Shen, H. Y. Wu, D. Y. Li, B. R. Li, J. L. Liang, X. Tang, J. Zhao, H. P. Li and P. W. Huo, *Chin. J. Struct. Chem.*, 2023, **42**, 100194.
34 L. X. Ma, Y. P. Gao, B. Q. Wei, L. Huang, N. Zhang, Q. Weng, L. Zhang, S. F. Liu and R. B. Jiang, *ACS Catal.*, 2024, **14**, 2775–2786.
35 Q. Zhang, M. Yue, P. Chen, Q. M. Ren, W. H. Kong, C. X. Jia, Q. Y. Lu, J. Z. Wu, Y. Q. Li, W. L. Liu, P. Li, Y. M. Fu and J. Ma, *J. Mater. Chem. C*, 2024, **12**, 3437–3449.
36 S. Y. Che, X. Y. Zhou, L. Zhang, D. W. Su, T. Y. Wang and C. Y. Wang, *Chem.–Asian J.*, 2022, **17**, 20220095.
37 H. Liu, S. X. Liu, X. Y. Zhou, L. Zhang, S. Zhu, Y. Zhang, T. Y. Wang and C. Y. Wang, *J. Catal.*, 2024, **430**, 115320.
38 X. Zhang, H. S. Chen, S. P. Jiang and P. Yang, *Nano Energy*, 2024, **120**, 109160.
39 S. Rao, C. Zhi, X. Wang, J. Su, Y. Sun, Y. Sun, R. Ma, Q. Liu, J. Yang and Z. Sun, *J. Colloid Interface Sci.*, 2024, **659**, 594–602.
40 L. Zhang, M. Jiang, H. Tian, S. X. Liu, X. Y. Zhou, H. Liu, S. J. Gan, S. Y. Che, Z. Chen, Y. Li, T. Y. Wang, G. X. Wang and C. Y. Wang, *ACS Sustain. Chem. Eng.*, 2024, **12**, 2028–2040.
41 Y. Shivamurthy Ravindra, S. Harikaranahalli Puttaiah, M. Gordon, S. Behzad, M. Afshin and Y. Kaan, *Chem. Eng. J.*, 2021, **426**, 131729.
42 X. Qi, Z. Zhao, N. Li, Z. He, Y. Chen and T. Jin, *New J. Chem.*, 2023, **47**, 3140–3150.
43 İ. Aksoy Çekceoğlu, Z. Eroğlu, E. Genc Acar, H. M. Kaya, E. Aslan, Ö. Metin and I. Hatay Patir, *ACS Appl. Nano Mater.*, 2024, **7**, 15720–15734.
44 Q. Xin, H. Shah, A. Nawaz, W. Xie, M. Z. Akram, A. Batool, L. Tian, S. U. Jan, R. Boddula, B. Guo, Q. Liu and J. R. Gong, *Adv. Mater.*, 2019, **31**, 1804838.
45 H. Liu, X. Zhou, L. Zhang, S. Zhu, Q. Yang, T. Wang, Y. Zhang and C. Wang, *Sep. Purif. Technol.*, 2025, **359**, 130684.
46 Y. Zhang, H. Li, X. Zhang, H. Zhang, W. Zhang, H. Huang, H. Ou and Y. Zhang, *J. Colloid Interface Sci.*, 2023, **630**, 742–753.
47 Z. Wu, X. He, Y. Xue, X. Yang, Y. Li, Q. Li and B. Yu, *Chem. Eng. J.*, 2020, **399**, 125747.
48 S. Sen, S. Ghosh, A. Jana, M. Jash, S. Ghosh, N. Mukherjee, D. Mukherjee, J. Sarkar and S. Ghosh, *ACS Appl. Bio Mater.*, 2024, **7**, 4142–4161.
49 S. Sen, R. Samat, M. Jash, S. Ghosh, R. Roy, N. Mukherjee, S. Ghosh, J. Sarkar and S. Ghosh, *J. Med. Chem.*, 2023, **66**, 11555–11572.